

Nanometer-sized, divalent-Mn, hydrous silicate domains in geothermal brine precipitates

ALAIN MANCEAU^{1,*} AND DARRELL L. GALLUP²

¹Environmental Geochemistry Group, Maison des Géosciences, University J. Fourier, BP 53, 38041 Grenoble Cedex 9, France

²Unocal Corporation, 1160 N. Dutton Avenue, Ste. 200, Santa Rosa, California 95401, U.S.A.

ABSTRACT

X-ray diffraction, infrared spectroscopy, and X-ray absorption (XANES and EXAFS) spectroscopy were combined to characterize poorly crystalline Mn-rich silicate scale deposited from brine at a geothermal field in Indonesia. The precipitate has a vitreous pink-amber appearance, a nearly pure SiO₂-MnO-H₂O chemical composition, and a bulk Mn/Si atomic ratio of 0.63. X-ray microfluorescence indicated that the sample consists of Mn-free and Mn-containing silica domains, whose Mn/Si ratio (1.2 ± 0.4) ranges between those of 2:1 and 1:1 phyllosilicates. The XRD pattern is characterized by a broad scattering band spanning from ~6 to ~2.5 Å with weak modulations at 5.3, 3.5, and 2.72 Å, and a faint band at 1.605 Å. A surrogate was synthesized in an O₂-free atmosphere by mixing and aging at 150 °C an MnCl₂ and a sodium meta-silicate solution for 3 hours. Its XRD pattern was similar to the scale sample, but the two reflections at 2.72 and 1.605 Å were enhanced and the former was asymmetrical as in randomly stacked layered compounds. Diffraction data are consistent with a mixture of amorphous silica and a poorly ordered manganous sheet silicate with a domain size of 40–50 Å for the scale and 50–60 Å for the surrogate material. The divalent oxidation state of manganese was confirmed by XANES spectroscopy, and the presumed existence of trioctahedral [Mn²⁺]₃(O,OH) clusters having a clay-like local structure was corroborated by the existence of a weak vibration band at 600–650 cm⁻¹ in infrared spectra. The connectivity of Mn octahedra was examined using EXAFS spectroscopy by comparing the local structure of Mn in the scale sample and in a large series of Mn compounds having different kinds of Mn octahedra and Si tetrahedra linkages. The manganous scale has a polyhedral local structure resembling that of sheet silicates, in which metal octahedra are joined along edges and share corners with ditrigonal SiO₄ rings. Similar short-range ordering has been described in Fe- and Al- silicate scales, but the Mn-silicate scale has a lower domain size owing to the greater misfit between the lateral dimensions of the Mn and Si sheets. The strain induced by the shrinkage of the Mn sheet to fit the Si sheet(s) is alleviated by the nanometer size of the two-dimensional hydrous silicate domains.

INTRODUCTION

Geothermal energy has been exploited for several decades as a renewable energy source. Both dry steam and hot water reservoirs are used to generate electricity or for space heating. In hydrothermal reservoirs, the water is usually in equilibrium with associated rocks and minerals, resulting in significant dissolved constituents. Total dissolved element concentrations in geothermal brines commonly range from 0.5 to 20 wt%. When these brines are brought to the surface through wells, the flashpoint of steam is reached. The flashing process decreases the temperature and pressure of the brines, while concentrating the dissolved solids. Consequently, flashing usually results in the supersaturation of some dissolved species followed by their precipitation and deposition as scale on any surfaces with which they come into contact. Scales can plug conduits, heat exchangers, wells, and the subterranean formation in the vicinity of brine disposal wells.

An especially troublesome component of hot brine is silica.

Prior to tapping the geothermal resource, the brine is generally saturated with respect to quartz and other silica-bearing minerals. The form of dissolved silica in brine is usually mono-silicic acid, Si(OH)₄. Because of flashing, the decrease of temperature and the increase of the concentration of Si(OH)₄ often results in exceeding the solubility of silica and leading to the scale deposition of amorphous silica owing to more rapid precipitation than other silica polymorphs; i.e., quartz, cristobalite, and tridymite (Fournier 1985). Nearly pure amorphous silica may deposit from low salinity brines. However, amorphous silica is often contaminated with metals in higher salinity brines. The most common metal silicate scales encountered in geothermal brine-handling systems are Fe and Al silicates (Manceau et al. 1995; Gallup 1998). At a geothermal field in Indonesia, we recently encountered a vitreous pink-amber precipitate in a brine-handling facility. The scale appeared downstream of a flashing vessel where the brine pH was ca. 8.0, the temperature was 152 °C and the pressure was 690 kPa. The scale adhered to piping much more tightly than any previously observed scale. Chemical analysis revealed that this scale contained 46.9 wt% SiO₂ and 34.8 wt% MnO, thereby rendering its pink color. The

* E-mail: manceau@ujf-grenoble.fr

unusually high Mn content of this scale was of interest. To improve our understanding of metal-silicate scaling mechanisms and the current technology of scale inhibition, we examined the mineralogy of the scale and some related phases.

MATERIALS AND METHODS

Geological setting and geochemistry of hydrothermal fluids

The hydrothermal field is located in an active volcanic range in Indonesia. The regional stratigraphy begins with a thick Paleozoic metasedimentary sequence, consisting of regionally metamorphosed meta-argillite, quartzite, and marble, which has been intruded in places by a series of Mesozoic granitic plutons. These basement rocks are overlain by Tertiary marine sedimentary rocks. The Tertiary sediments are in turn capped by voluminous Neogene and Quaternary volcanic and volcanoclastic rocks associated with the volcanic arc. Much of the volcanism is andesitic in composition, but the Quaternary arc is characterized by voluminous rhyolitic ash-flow tuffs. The silica volcanism is associated with elevated regional heat flow and crustal uplift. The most recent volcanic unit in the field is a biotite dacite lava with a glassy texture and flow-banding structure.

The extraction well was drilled to a depth of 1722 m. The well fluid composition is given in Table 1. The reservoir brine pH is estimated to be about 5.5 at 287 °C. Upon transport to the surface, flashing of the highly enriched bicarbonate brine causes the pH to increase to 7.5–8.5 at 152 °C. Calcite scaling in the production well is nonexistent owing to the low Ca concentration in the brine. Amorphous silica is slightly undersaturated in the wellbore, but flashing to the elevated pH range drives deposition of silica together with Mn on surface pipping and reinjection brine well bore pipes. The enrichment of Mn in the brine, compared with most other geothermal systems, is believed to be related to the slightly acidic reservoir fluid leaching the metal from the sedimentary marine rocks, preferentially to Ca and Mg. Modeling suggests that Mn occurs in the brine as a bicarbonate complex (Spycher and Reed 1989). In most geothermal brines, Mn does not precipitate directly with silica. In this unusual geothermal system, however, Mn²⁺ is sufficiently prevalent relative to Mg²⁺, Ca²⁺, Fe²⁺, and Al³⁺ to form almost pure Mn-silicate scale.

Description of samples studied

The scale sample is hard and has a vitreous luster. A 30 μm-thick polished thin section was examined with a polarizing microscope. The sample is transparent with a 1st-order gray birefringence colors as for silica. However, in contrast to silica, the matrix has a general pink tint, and grains have an acicular shape. The color intensity is inhomogeneous, being more pronounced in millimeter-wide veinlets. An average sample was ground in an agate mortar for infrared (IR), X-ray diffraction (XRD), and extended X-ray absorption fine-structure (EXAFS) measurements. Major elements were analyzed by inductively coupled plasma atomic emission spectroscopy (ICP-AES) and trace elements by inductively coupled plasma mass spectroscopy (ICP-MS). Six reference samples were also studied: pyrochroite [Mn(OH)₂], poorly crystalline Mn(II)-phyllosilicate, tephroite (Mn₂SiO₄), pyroxmangite (MnSiO₃), rhodonite (MnSiO₃), and manganpyrosomalite [(Mn,Fe)₈Si₆O₁₅(OH,Cl)₁₀].

The poorly crystalline Mn(II)-phyllosilicate was prepared as follows: 20 mL of 1.59 M MnCl₂ solution and 300 mL of 0.02 M sodium meta-silicate (SiO₂Na₂O) solution were placed into a 1 L Hastelloy C-276 pressure reactor. The Mn:Si mol ratio of the reactants was set at 3:4. The headspace in the reactor was filled with nitrogen to prevent Mn²⁺ oxidation. The reaction mixture was heated to 150 °C with stirring for 3 hours, and the final pH was 10.1. The mixture was removed from the reactor into a glove bag filled with N₂ and through a cooling coil to prevent flashing. Next, the precipitate was filtered through a Whatman #1 (11 μm) paper, washed with distilled water, and dried overnight under N₂ atmosphere. The synthetic phase was pink in color, indicating that the Mn remained in a reduced state.

Analyses

IR analysis was performed on an ATI / Mattson Research Fourier transform (FT)-IR spectrometer (resolution 5 cm⁻¹). Spectra were recorded in transmission mode on pellets in a KBr matrix. The XRD measurement was performed on a Siemens D5000 diffractometer using CuKα X-ray and a Si/Li solid-state detector. The data were collected in step-scan mode with a step interval of 0.04° and a counting

time of 15 s/point. Mn K-edge X-ray absorption near-edge structure (XANES) and powder extended X-ray absorption fine structure (EXAFS) spectra were collected at ambient temperature and in transmission mode on the D42 station at the LURE synchrotron facility at Orsay, France. An Si(331) channel-cut monochromator was used. Gas ionization chambers contained an Ar/He mixture to attenuate the beam intensity by ~20% before and ~50% after the samples. The absolute energy of the spectra was referenced to the first inflection point of elemental Mn (6539 eV).

All XANES spectra were normalized to unit step in the absorption coefficient from below the edge to the middle of the first EXAFS oscillation. Both EXAFS and XANES data were reduced and analysed using WinXAS (Ressler 1998). Radial structure functions (RSFs) were obtained by the Fourier transform of k³-weighted normalized EXAFS spectra from the reciprocal k space to the distance R space. RSFs were not corrected for EXAFS phase-shifts, causing peaks to appear at shorter distances (R + ΔR, with Δ ~ -0.3 to -0.4 Å) relative to the true near-neighbor distance (R). Each peak in the RSF was then isolated and back-transformed for atomic shell analysis. Partial EXAFS spectra (χ_o, χ_{Mn}, and χ_{Si} functions) were fitted by least-squares with theoretical phase shift and amplitude functions calculated *ab initio* with the FEFF 7.02 code (Rehr et al. 1991). Fits were optimized by minimizing the residual parameter Res defined as:

$$Res = \frac{\sum_{i=1}^j |\chi_{exp}(i) - \chi_{theo}(i)|}{\sum_{i=1}^j \chi_{exp}(i)} \cdot 100$$

where j is the number of points in the fit window, and χ_{exp} and χ_{theo} are the experimental and theoretical partial EXAFS functions. The S₀² scaling factor was calibrated with pyrochroite for the Mn shell, and with tephroite for the Si shell. From the comparison between EXAFS and crystallographic data of the standards, the absolute accuracy in interatomic distance (R) and coordination number (N) values is typically ± 0.03 Å and ± 30%. The relative precision is better.

RESULTS

Chemical composition

The mass concentrations of major elements in the scale sample are (in wt%): SiO₂ = 46.9, MnO = 34.8, Al₂O₃ = 1.6, Fe₂O₃ = 0.9, MgO = 0.8, Na₂O = 0.7, K₂O = 0.6, CaO = 0.4, P₂O₅ = 0.3, and the loss on ignition is 13.7. The sum of all other elements amounts to less than 0.1 wt%. In addition to Si and Mn, this sample contains significant structural water/OH (<~10 wt%) in an amount higher than in amorphous silica (Graetsch 2002). The scale sample is thus a nearly pure SiO₂-MnO-H₂O compound with a bulk Mn/Si atomic ratio (0.63) similar to sepiolite (0.67), and lower than trioctahedral 1:1 (1.5, e.g., serpentine) and 2:1 phyllosilicates (0.75, e.g., talc), and higher than palygorskite (0.5). The homogeneity of Mn in the sample was investigated by X-ray microfluorescence on the 10.3.2 spectrometer of the Advanced Light Source (LBNL, Berkeley). A 4 × 4 mm area of the 30 μm-thick thin section examined by optical microscopy was scanned under a 10 keV X-ray beam at 7 × 7 μm resolution, while recording the MnKα X-ray fluorescence (data not shown). About 50 % of the mapped area contained only Si, and in the other half the intensity of the MnKα line varied by a factor two. Therefore, the actual Mn/Si ratio in the Mn-containing area is about 1.2 ± 0.4, and ranges between the stoichiometry of 2:1 and 1:1 phyllosilicates. The chemical composition of the synthetic manganous hydrous silicate is (in wt%) SiO₂ = 45.7, MnO = 40.5, Fe₂O₃ = 0.18, MgO = 0.10, Na₂O = 2.21, CaO = 0.28, and ignition loss = 8.8. The Mn and Si are in 0.75 ratio, as expected from the composition of the mother solution.

TABLE 1. Brine composition (mg/kg)

Li	B	HCO ₃ ⁻	F	Na	Mg	Al	SiO ₂	SO ₄ ²⁻	Cl	K	Ca	Mn	Fe	Total dissolved solid
5.4	15	260	3	359	0.5	<0.1	735	162	466	81	2.4	21	0.1	2150

XRD

The XRD pattern of the scale sample is characterized by a prominent broad hump centered at about 3.5 Å with three weak intensity maxima at 5.3, 3.5, and 2.72 Å, and a faint reflection at 1.605 Å (Fig. 1). The broad scattering feature at 15–30 °2θ is attributed to amorphous silica. If present, opal-A is probably very minor because it has a broad and featureless scattering band at 4.1 Å (Jones and Segnit 1971). The bands at 2.72 Å and 1.605 Å are also observed in the synthetic hydrous Mn silicate. We assume that the two bands arise from the same structural unit in the scale and synthetic compounds. The peak at 1.605 Å is attributed to the 06-33 reflection and that at 2.72 Å to the 20-13 reflection of disordered layer silicates (orthogonal layer setting). The asymmetry of the 2.72 Å peak on its high-angle side is believed to arise from the residual 02*l* and 11*l* reflections in layer minerals lacking three-dimensional periodicity (Brindley and Brown 1980). In Mn(OH)₂, the 06-33 and 20-13 reflections (or 110 and 100 in hexagonal layer setting) are at 1.66 and 2.87 Å. The reduction of the *d*(*hkl*) values in the Mn-Si scale is consistent with manganous hydrous silicate structural units because the lateral dimension of an Mn-rich octahedral sheet in phyllosilicates is reduced to relieve the misfit with the attached tetrahedral sheet(s) (Guggenheim and Eggleton 1987, 1988). The absence of visible 02-11 band at about 1.605 × 3 = 4.8 Å (18.4 °2θ) is explained by the sample composition because the I(20-13)/I(02-11) ratio in c*-disordered trioctahedral phyllosilicates depends on the chemical composition of the octahedral sheet, and is a maximum for 3d transition elements. For example, in pure Zn-smectites the 02-11 band is about 10 times less intense than the 20-13 band (Decarreau 1985; Gallup et al. 2003). Consequently, the XRD pattern of the unknown sample provides suggestive evidence for poorly crystalline hydrous Mn silicate domains having a two-dimensional extension. The full width at half maximum (FWHM) of the 06-33 reflections were used to estimate the particle size using the Debye-Scherrer formula $t = 0.9\lambda/B\cos\theta_B$, where *t* is the size of the grain (actually the average dimension of coherent scattering domains), λ is the wavelength of X-ray used (CuKα = 1.542 Å) and θ_B is Bragg's angle. *B* was calculated from the equation $B = (B_m^2 - B_s^2)^{1/2}$, where *B_m* is the FWHM of the sample and *B_s* is the FWHM of a well-crystallized standard used to correct instrumental broadening. Domain sizes obtained for the scale and surrogate materials are 40–50 and 50–60 Å, respectively. The higher domain size of the laboratory-derived surrogate is consistent with the enhanced intensity

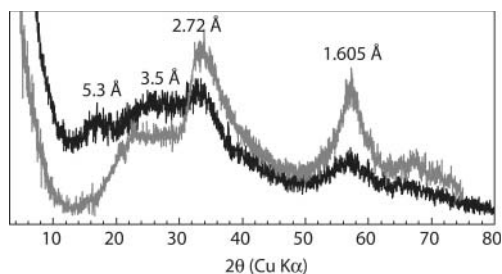


FIGURE 1. Experimental powder X-ray diffraction pattern of the scale sample (black line) and the synthetic divalent-Mn, hydrous silicate (gray line).

of the 06-33 and 20-13 reflections in this sample (Fig. 1). The glassy texture of the scale sample hampered the preparation of oriented aggregates to reinforce the contribution from 00*l* reflections on the XRD pattern.

IR

The scale and synthetic Mn-silicate samples have similar IR patterns with main absorption bands at 3450 (not shown), 1650, 1000, 600–650, and 450 cm⁻¹ (Fig. 2). The bands at 3450 and 1650 cm⁻¹ are related to water molecules, and the bands at 1000 and 450 cm⁻¹ are common to all silicates with tetrahedrally coordinated Si (Etchepare et al. 1974; Moenke 1974; Etchepare et al. 1978). Although the two IR spectra present some similarities with that of noncrystalline silica (e.g., opal-A), distinct differences are noted. The prominent Si-O-Si bending band at 1000 cm⁻¹ is significantly shifted relative to that of silica minerals (~1100 cm⁻¹). In silica, only low-cristobalite and opal-C have an absorption band at ~650 cm⁻¹ as observed experimentally here (Etchepare et al. 1978). However, this mineral species assignment is disregarded because no crystalline opal was detected by X-ray diffraction and because cristobalite and opal-C have an intense band at 800 cm⁻¹ (Graetsch et al. 1994), which is not present in the scale sample. Instead there is a striking spectral resemblance to sepiolite (Wollast et al. 1968; Nagata et al. 1974; Yenyol 1986; Webb and Finlayson 1987). The ~650 cm⁻¹ band of sepiolite was ascribed to the [Mg]₃OH deformation modes (Russell et al. 1970). The position of this band is nearly independent of the nature of the octahedral cation (Wilkins and Ito 1967; Gerard and Herbillon 1983; Decarreau et al. 1987, 1992), and supports the possible existence of trioctahedral [Mn²⁺]₃OH clusters inferred from XRD data. The IR data also suggest that the hydrous Mn-silicate domains have a 2:1 local structure because the intensity ratio of the 650 to 450 cm⁻¹ bands is low in 2:1 clays and high in 1:1 clays (Kermarec et al. 1994).

XANES spectroscopy

The XANES spectra of the scale and synthetic Mn-silicate samples are compared to Mn²⁺ [Mn(OH)₂], Mn³⁺ (β-MnOOH), and Mn⁴⁺ (ramsdellite, MnO₂) references in Figure 3. As reported in other studies, the energy of the edge position increases with the formal valence (Bargar et al. 2000; Manceau et al. 2000). The position in energy of the two Mn silicates coincides with that of the Mn²⁺ reference indicating that Mn is divalent. This result is consistent with the pink color of the two samples under

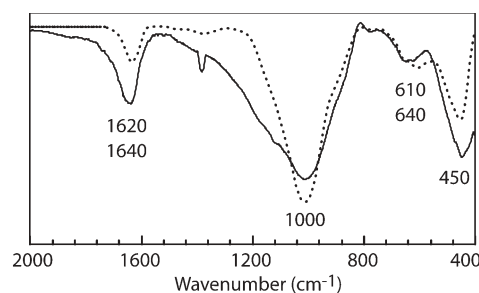


FIGURE 2. Infrared spectrum of the scale sample (solid line) and the synthetic divalent-Mn hydrous silicate (dotted line).

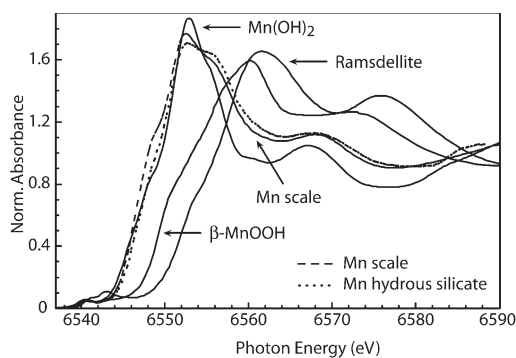


FIGURE 3. Mn *K*-edge XANES spectra of the scale sample and the synthetic divalent-Mn hydrous silicate together with Mn²⁺ [Mn(OH)₂], Mn³⁺ (β-MnOOH), and Mn⁴⁺ (ramsdellite, MnO₂) references.

transmitted light (Rossman 1988), and with the assignment of the infrared band at 600–650 cm⁻¹.

EXAFS spectroscopy

The EXAFS patterns of the two Mn-silicate samples are obviously similar (Fig. 4a). The multiple wave frequencies and structured shape of the EXAFS spectra contrasts with the essentially featureless nature of the XRD traces, and indicate that the Mn environment involves short-range order but long-range disorder. In Fourier space (Fig. 4b), two intense peaks are shown at low distance (labeled A and B) and weaker, but significant, atomic shell peaks at higher distance (labeled C, D, and E). The first peak arises from the O coordination shell about Mn atoms and the second is so intense that it should result (at least partly) from Mn nearest neighbors. Both the height of the first metal shell peak, and the presence of higher distance peaks in the Fourier transform at $R + \Delta R \sim 4.0, 5.0,$ and 6.5 \AA , indicate that the size of the Mn structural entities is at least a few tens of angstroms (Manceau and Calas 1986).

Usually, the nature of cations located in the immediate vicinity of the probed atom (here Mn) and the connectivity of metal polyhedra are determined by simulating the unknown EXAFS spectrum with plausible atomic pairs (here Mn-Mn and Mn-Si on the basis of chemical analysis) until a satisfactory spectral fit is obtained. As with any fitting technique, there are concerns about the uniqueness of the analysis, especially when the matrix contains light atoms, such as Si, because of their weak scattering contribution relative to transition metals. In the case of hydrous layer silicates, this difficulty is avoided by polarized EXAFS, but this technique is not applicable here because the material under study is not anisotropic. Therefore, the local structure of the unknown sample was compared with those of a selection of reference compounds. As shown below, the nature of the cations located in the immediate vicinity of Mn atoms could be identified, and the connectivity of Mn and Si polyhedra determined, with a good level of confidence.

Mn(OH)₂-like local structure

One of the simplest divalent Mn compounds is Mn(OH)₂, which consists of Mn(OH)₆ octahedra linked by edges in a two-dimensional framework (Norlund 1965) (Fig. 5a). RSF peaks for Mn(OH)₂ are assigned by comparison with Co(OH)₂ because the

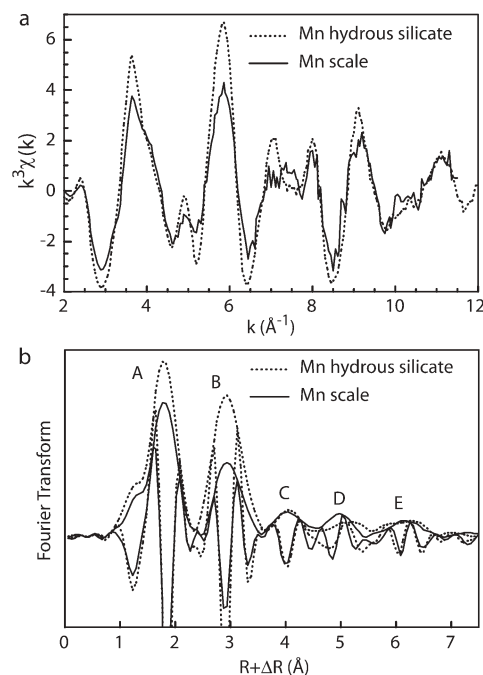


FIGURE 4. Mn *K*-edge EXAFS spectra (a) and Fourier transforms (b) of the scale sample and the synthetic divalent-Mn hydrous silicate. In (b), the envelope curve is the magnitude of the complex Fourier transform $[(R^2+I^2)^{1/2}]$ and the oscillatory curve is the imaginary part of the transform. The peak positions are not corrected for phase shift and, consequently, are shifted by $\Delta R \sim -0.3$ to -0.4 \AA relative to crystallographic *R* distances.

two hydroxides have the same layer structure (O'Day et al. 1994; Manceau et al. 1999). Peak A in Figure 5b arises from the oxygen ligand shell at 2.20 Å in Mn(OH)₂, peak B from the nearest Mn shell (Mn1) at 3.32 Å, peak D' from the second-nearest Mn shell (Mn2, 5.75 Å), and peak E' from the third-nearest Mn shell (Mn3, 6.64 Å). Peak E', which is located at twice the distance of peak B, is detected in trioctahedral layer structures because of the alignment of Mn-Mn1-Mn3 cations, which amplifies multiple scattering (MS) paths of the photoelectron. Conversely, this MS path is absent in dioctahedral structures owing to the existence of vacancies at the Mn1 position (Mn-□-Mn3) that break the focusing of the electronic waves (Manceau et al. 1998).

Comparing the peak positions and the imaginary parts of the Fourier transforms for the scale sample and Mn(OH)₂ in the $1.0 \text{ \AA} < R + \Delta R < 3.5 \text{ \AA}$ interval, we find that there is a leftward shift of the unknown (Fig. 5b). This indicates smaller interatomic distances. Spectral simulation yielded Mn-O distances of 2.18 Å ($N_O = 8, \sigma = 0.10 \text{ \AA}, \Delta E = 2.7 \text{ eV}, Res = 12$) in the scale sample and 2.21 Å ($N_O = 6, \sigma = 0.05 \text{ \AA}, \Delta E = 3.1 \text{ eV}, Res = 28$) in Mn(OH)₂. The EXAFS Mn-O distance for Mn(OH)₂ is in good agreement with x-ray diffraction (2.20 Å). According to EXAFS theory, the simultaneous shift to lower $R + \Delta R$ values of both the magnitude and imaginary part of the second RSF peak for the Mn scale relative to Mn(OH)₂ indicates that the second shell of the unknown contains the same atom as in the reference (i.e., Mn), and that the interatomic distance is shorter. This interpretation was confirmed by spectral simulation after singling out and back-

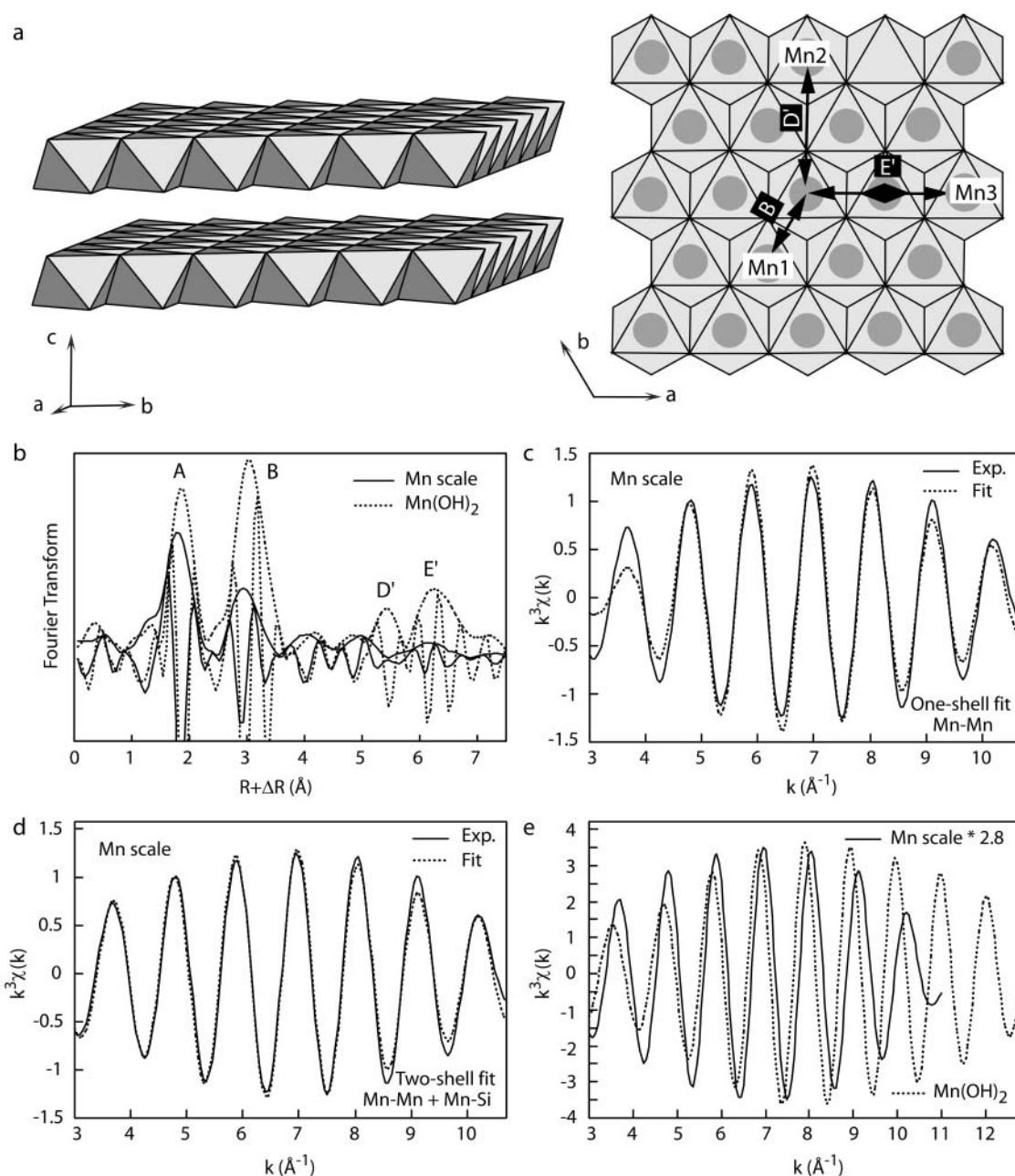


FIGURE 5. (a) Polyhedral sketch of the structure of $\text{Mn}(\text{OH})_2$ and projection of the structure onto the a - b plane with representation of the Mn-Mn1, Mn-Mn2, and Mn-Mn3 pairs and illustration of the Mn-Mn1-Mn3 focusing effect. (b) Fourier transforms of the Mn-EXAFS spectra for the scale sample and $\text{Mn}(\text{OH})_2$. Peak A corresponds to the Mn-O pair, peak B to the Mn-Mn1 pair, peak D' to the Mn-Mn2 pair, and peak E' to the Mn-Mn3 pair. The amplitude of peak E' is enhanced by the alignment of Mn, Mn1, and Mn3 (multiple scattering path of the photoelectron). (c) One-shell fit of the electronic wave from peak B for the scale sample assuming $N_{\text{Mn1}} = 4.2$, $\sigma = 0.10 \text{ \AA}$, and $R_{\text{Mn1}} = 3.27 \text{ \AA}$. (d) Two-shell fit assuming $N_{\text{Mn1}} = 5.0$, $\sigma = 0.10 \text{ \AA}$, $R_{\text{Mn1}} = 3.27 \text{ \AA}$, $N_{\text{Si1}} = 3.8$, $\sigma = 0.10 \text{ \AA}$, $R_{\text{Si1}} = 3.34 \text{ \AA}$. The $R + \Delta R$ window for the inverse Fourier transform is $[2.5\text{--}3.6] \text{ \AA}$. (e) Fourier-filtered contributions to EXAFS of the nearest cationic shells for the scale sample and $\text{Mn}(\text{OH})_2$.

transforming to k space the two metal shell RSF peaks. A fair spectral simulation ($Res = 22$) of the Mn-Mn1 shell in the scale sample was obtained assuming 4.2 Mn atoms ($\sigma = 0.10 \text{ \AA}$) at 3.27 \AA (Fig. 5c, Table 2). From geometrical considerations, this distance is related also to edge-sharing divalent Mn octahedra. This structural model, however, provided only an approximate fit to the partial EXAFS spectrum at $k < 4.5 \text{ \AA}^{-1}$. Because the

wave amplitude of light atoms is maximum at low k (Teo 1986), the spectral mismatch in this region is suppressed ($Res = 13$) by adding a second cationic shell consisting of Si atoms at 3.34 \AA (Fig. 5d, Table 2). This possible structural interpretation is supported by the overlay plot of the scale sample and $\text{Mn}(\text{OH})_2$ metal contributions, which shows that the two waves effectively have a differing envelope at low k , suggesting the existence of

TABLE 2. EXAFS parameters for Mn and Si shells

Sample	Mn-Mn			Mn-Mn			Mn-Si			ΔE (eV)	Res	
	R (Å)	N	σ (Å)	R (Å)	N	σ (Å)	R (Å)	N	σ (Å)			
Mn(OH) ₂	3.34	6.0*	0.06	—	—	—	—	—	—	6.7	6	
Mn scale	One-shell fit	3.27	4.2	0.10	—	—	—	—	—	5.2	22	
	Two-shell fit	3.27	5.0	0.10†	—	—	3.34	3.8	0.10†	2.0	13	
Rhodonite	One-shell fit	3.38	3.4	0.10	—	—	—	—	—	6.1	33	
	Two-shell fit	3.39	4.9	0.09	—	—	3.43	5.3	0.09	0.8	15	
	Average XRD value‡	3.37	4.6	—	—	—	3.39§	5.0	—	—	—	
Pyroxmangite	Two-shell fit	3.21	7.4	0.14†	3.41	5.4	0.14†	—	—	5.9	23	
	Three-shell fit	3.18	2.6	0.11†	3.40	5.0	0.11†	3.42	6.4	0.11†	0.8	15
	Average XRD value‡	3.31	4.6	—	—	—	3.41	5.4	—	—	—	
Pyrosmalite	Two-shell fit	3.27	4.2	0.07†	3.43	4.8	0.07†	—	—	5.4	20	
	Three-shell fit	3.25	2.6	0.04†	3.42	5.6	0.04†	3.44	4.2	0.04 ²	2.1	8
	Average XRD value#	3.37	6.0	—	—	—	3.40	2.7	—	—	—	

* Held fixed to the crystallographic value.

† Constrained to be identical for all subshells.

‡ After Narita et al. (1977).

§ $R(\text{Mn-Si})_{\text{edge}} = 2.97 \text{ \AA}$, $N(\text{Mn-Si})_{\text{edge}} = 0.6$.

|| $R(\text{Mn-Si})_{\text{edge}} = 2.95 \text{ \AA}$, $N(\text{Mn-Si})_{\text{edge}} = 0.6$.

After Takéuchi et al. (1969).

an additional shell in the scale (Fig. 5e). Still, this structural interpretation is not robust, and additional support for the existence of Mn-Si pairs is provided below. Attempts to simulate the experimental wave function with an Mn shell at about 3.3 Å together with a second O shell at 3.8 to 4.1 Å instead of Mn-Mn + Mn-Si pairs failed. This result may be explained by the high disorder of the O2 shell in Mn silicates (Takéuchi et al. 1969; Narita et al. 1977).

The reduction of amplitude of the metal shell peaks B, D, and E in the scale sample originates from structural disorder as indicated by the relatively high Debye-Waller value (σ) of the Mn1 shell (0.10 Å). In the spectral simulation, the distribution of distance was modeled by assuming a Gaussian fit, and the Mn1 shell was best fit by 5 Mn (in the two-shell fit, Table 2) located at an average distance of 3.27 Å with a continuous distribution of 0.10 Å half-width. The distribution of the Mn-Mn1 distances is too small to resolve, and the fit would be improved insignificantly by assuming two discrete Mn-Mn distances (i.e., a bimodal distribution). This contrasts with the analysis of the $\chi_{\text{Mn-Mn1}}$ functions for pyroxmangite and pyrosmalite, because in these minerals, a wave beating occurs at $k = 8 - 10 \text{ \AA}^{-1}$, and the spectral simulations required two Mn sub-shells separated by $\Delta R = \pi/(2k) = 0.16 - 0.20 \text{ \AA}$ (see below). The relatively limited local disorder of the scale sample is consistent with the hypothesis of small ordered trioctahedral Mn domains, because the disorder only arises from border Mn atoms (higher order Mn-Mn correlations at grain boundaries are obviously weakened).

Olivine-like local structure

Now that the presence of edge-sharing Mn-Mn octahedra in the scale sample has been established, the possibility of edge-sharing between Mn octahedra and Si tetrahedra in a manner analogous to olivine is considered next. In addition to tephroite (Mn₂SiO₄), olivine-like polyhedral connectivity occurs in minerals from the humite and leucophoenicite group, whose Mn-rich members include jerrygibbsite [Mn₉(SiO₄)₄(OH)₂], alleghanyite [Mn₅(OH)₂(SiO₄)₂], ribbeite [Mn₅(OH)₂(SiO₄)₂], and leucophoenicite *sensu stricto* [Mn₇(SiO₄)₂SiO₄(OH)₂] (Moore 1970; Freed et al. 1993). A polyhedral diagram of a portion of the structure common to these minerals and the RSF of tephroite are presented in Figure 6a. The Mn-Si distance across the shared edge typically

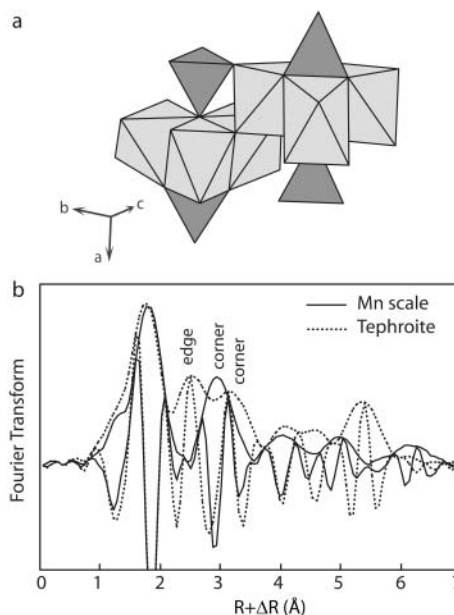


FIGURE 6. (a) Polyhedral sketch of a portion of the structure common to mineral species from the olivine-, humite-, and leucophoenicite-group of minerals. SiO₄ tetrahedra (dark gray) are linked by edges and corners to MnO₆ octahedra (light gray). After Fujino et al. (1981). (b) Comparison of the Fourier transforms for the scale sample and tephroite.

ranges between 2.8 and 2.9 Å, and this atomic pair produces a pronounced peak after the Mn-O peak (Fig. 6b). The second metal-shell peak in the RSF of tephroite corresponds to the admixture of the Mn-Mn_{edge} and Mn-Si_{corner} pairs. The comparison of the RSFs for tephroite and the scale sample demonstrates that the olivine-type of polyhedral association is not present in the scale sample.

Pyroxenoid-like local structure

This mineral group has the same connectivity of polyhedra as in the olivine-type group, but a different topology (Fig. 7a, 8a). Pyroxenoids are single-chain silicates (like pyroxenes) and, hence, differ at the local scale from the olivine-type group by the relative number of Mn-Si_{edge} to Mn-Si_{corner} linkages. Whereas in the olivine group each Mn octahedron shares on average 1.5

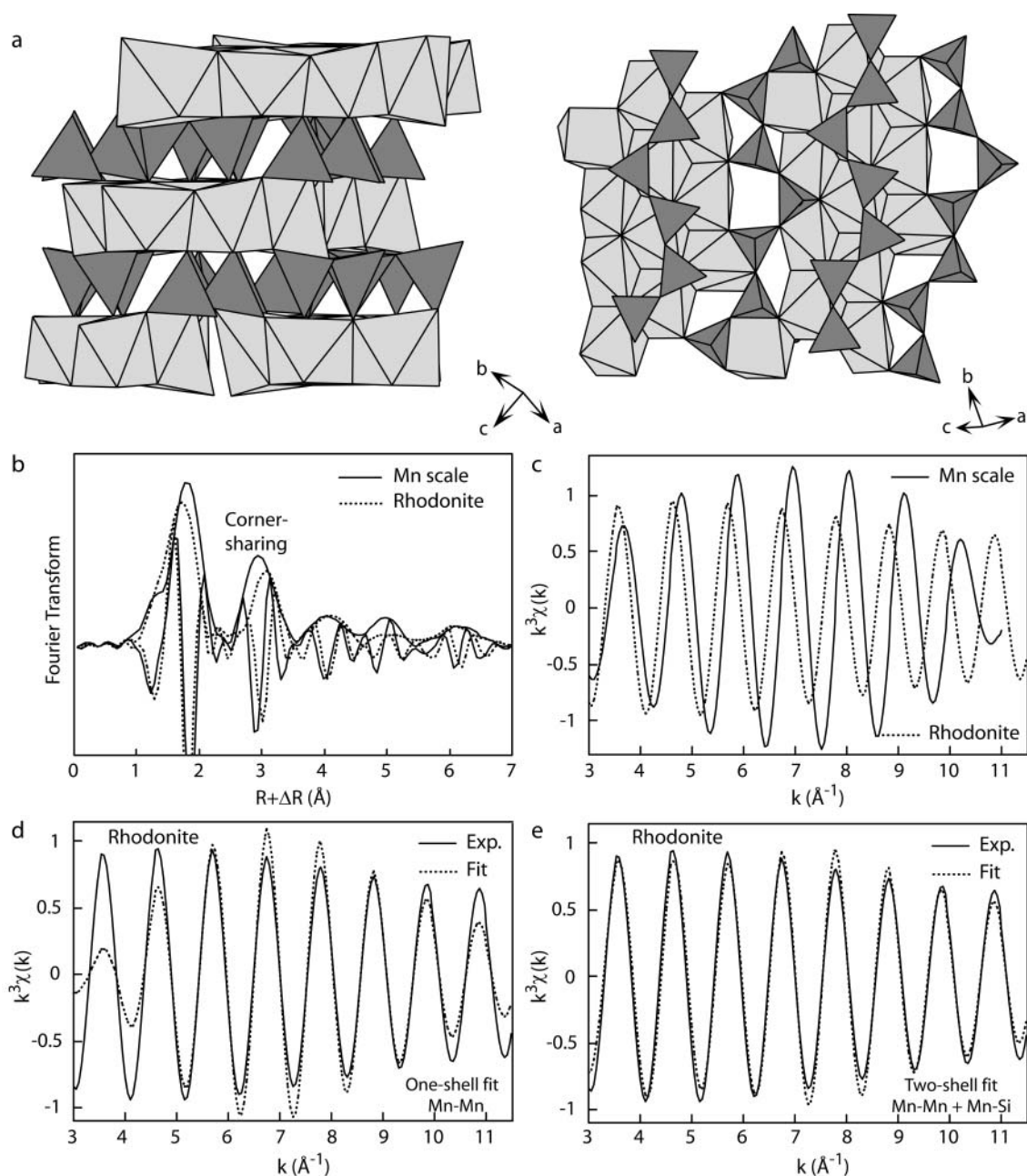


FIGURE 7. (a) Polyhedral representations of the rhodonite (MnSiO_3) structure showing the layer structure (left sketch) and the MnO_6 ribbons (light gray) and the kinked SiO_4 single chains (dark gray, right sketch). After Narita et al. (1977). In rhodonite, the periodicity of the SiO_4 , pyroxene-like, single-chains is 5. The octahedral Mn bands of manganoan pyroxenoids contain two different kinds of sites, those on the inside of the bands and those on their edges. The inner octahedra share corners with SiO_4 tetrahedra, whereas the Mn octahedra on the edges of the bands share edges and corners with SiO_4 tetrahedra. The various coordinations of the Mn octahedra result in a considerable scatter of interatomic distances. (b) Comparison of the Fourier transforms for the scale sample and rhodonite. (c) Fourier-filtered contributions to EXAFS of the nearest cationic shells for the scale sample and rhodonite. (d) One-shell fit for rhodonite assuming $N_{\text{Mn1}} = 3.4$, $\sigma = 0.10 \text{ \AA}$, and $R_{\text{Mn1}} = 3.38 \text{ \AA}$. (e) Two-shell fit for rhodonite assuming $N_{\text{Mn1}} = 4.9$, $\sigma = 0.09 \text{ \AA}$, $R_{\text{Mn1}} = 3.39 \text{ \AA}$, $N_{\text{Si1}} = 5.3$, $\sigma = 0.09 \text{ \AA}$, $R_{\text{Si1}} = 3.43 \text{ \AA}$. The $R + \Delta R$ window for the inverse Fourier transform is $[2.7\text{--}3.6] \text{ \AA}$.

edges with Si tetrahedra, in the pyroxenoid group the average number of Mn-Si_{edge} linkages per Mn octahedron is significantly lower. In rhodonite and pyroxmangite, this number equals 0.6 (Narita et al. 1977; Pinckney and Burnham 1988). Consequently, the short distance Mn-Si_{edge} peak observed in the tephroite RSF is not apparent on the RSF (Fig. 7b). Accordingly, this shell was

neglected during spectral simulations (Table 2). Conversely, the number of Mn-Si_{corner} linkages is higher in pyroxenoids, being equal to 5.0 in rhodonite and 5.4 in pyroxmangite compared to 3.0 in tephroite.

Figures 7b and 8b show that the RSF peaks have a lower amplitude in rhodonite and pyroxmangite than in the Mn scale

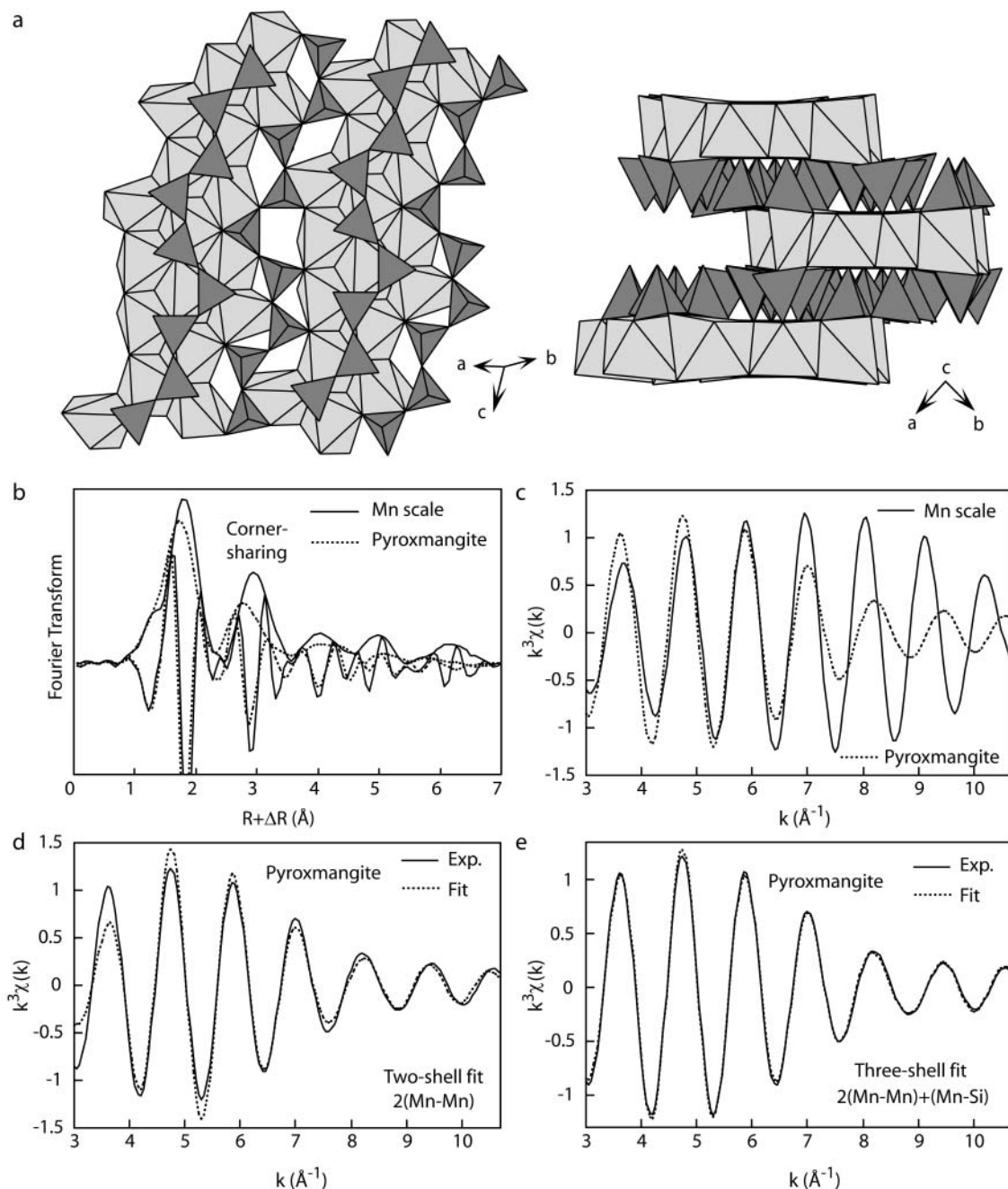


FIGURE 8. (a) Polyhedral representations of the pyroxmangite (MnSiO_3) structure showing the layer structure (left sketch), the MnO_6 ribbons (light gray), and the kinked SiO_4 single chains (dark gray, right sketch). In pyroxmangite, the periodicity of the SiO_4 , pyroxene-like, single-chains is 7. After Narita et al. (1977). (b) Comparison of the Fourier transforms for the scale sample and pyroxmangite. (c) Fourier-filtered contributions to EXAFS of the nearest cationic shells for the scale sample and pyroxmangite. (d) Two-shell fit for pyroxmangite assuming $N_{\text{Mn1a}} = 7.4$, $\sigma = 0.14 \text{ \AA}$, and $R_{\text{Mn1a}} = 3.21 \text{ \AA}$, $N_{\text{Mn1b}} = 5.4$, $\sigma = 0.14 \text{ \AA}$, and $R_{\text{Mn1a}} = 3.41 \text{ \AA}$. (e) Three-shell fit for pyroxmangite assuming $N_{\text{Mn1a}} = 2.6$, $\sigma = 0.11 \text{ \AA}$, and $R_{\text{Mn1a}} = 3.18 \text{ \AA}$, $N_{\text{Mn1b}} = 5.0$, $\sigma = 0.11 \text{ \AA}$, $R_{\text{Mn1a}} = 3.40 \text{ \AA}$, $N_{\text{Si1}} = 6.4$, $\sigma = 0.11 \text{ \AA}$, $R_{\text{Si1}} = 3.42 \text{ \AA}$. The $R + \Delta R$ window for the inverse Fourier transform is [2.3–3.5] \AA .

sample, despite the good crystallinity of the two references. This noteworthy feature results from the considerable scatter of interatomic distances in the two references owing to the band structure of the Mn layer and the strongly kinked nature of the tetrahedral chains. The octahedral bands contain basically two kinds of sites, those on the inside of the bands and those on

their edges. The inner octahedra share corners with apical oxygen atoms of a tetrahedral chain, whereas the outer octahedra share edges and corners with tetrahedra because of the lateral jog of the tetrahedral chains. One Mn shell proved sufficient to fit the frequency of the $\chi_{\text{Mn-Mn1}}$ function for rhodonite, but the wave envelope over the entire k range, and specifically for $k <$

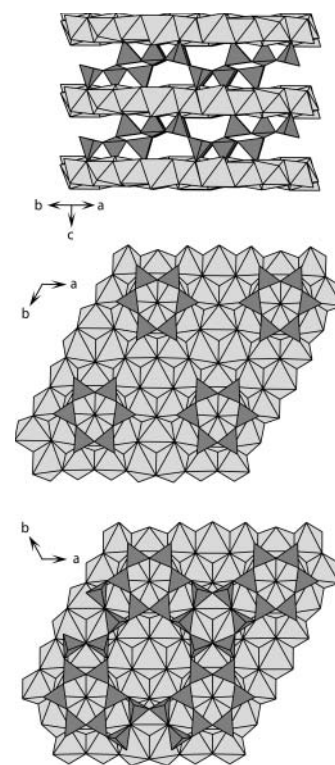
5 \AA^{-1} , was poorly reproduced, suggesting the contribution of Si atoms (Fig. 7d). Addition of this shell yielded a satisfactory fit, and the EXAFS distances ($R_{\text{Mn-Mn1}} = 3.39 \text{ \AA}$; $R_{\text{Mn-Si1}} = 3.43 \text{ \AA}$) were in good agreement with the average XRD distances ($R_{\text{Mn-Mn1}} = 3.37 \text{ \AA}$; $R_{\text{Mn-Si1}} = 3.39 \text{ \AA}$; Narita et al. 1977) (Fig. 7e). In contrast to rhodonite, a three-shell fit (two Mn-Mn1 and one Mn-Si1 pairs) was necessary to fit the contribution to EXAFS of the nearest cationic shells of pyroxmangite (Table 2, Figs. 8d-e). The addition of a second Mn shell is justified by the rapid damping of the wave amplitude at increasing k value, which only can be explained by the incoherence of the Mn-Mn distances. The wider dispersion of the Mn-Mn distances in pyroxmangite agrees with XRD data because its asymmetric cell contains seven independent Mn positions compared with five in rhodonite. The comparison of the $\chi_{\text{Mn-Mn}}$ functions for the Mn scale, $\text{Mn}(\text{OH})_2$, rhodonite, and pyroxmangite indicates that the structural order in the unknown is intermediate between $\text{Mn}(\text{OH})_2$ and pyroxenoids, and not distinctive of pyroxenoids.

Hydrous silicate-like local structure

The hydrous Mn silicate reference is manganpyrosomalite $[(\text{Mn},\text{Fe})_8\text{Si}_6\text{O}_{15}(\text{OH},\text{Cl})_{10}]$; Takéuchi et al. 1969]. This mineral has octahedral sheets of Mn joined together by tetrahedral Si sheets whose six-membered rings point alternatively in opposing directions (Fig. 9). The tilting of tetrahedra results from the difference in the lateral dimensions of the Mn and the Si sheets. Besides manganpyrosomalite, the structure of another modulated Mn layer silicate has been refined, bementite $[\text{Mn}_7\text{Si}_6\text{O}_{15}(\text{OH})_8]$ (Heinrich et al. 1994). The two minerals differ essentially by the size of rings of SiO_4 tetrahedra, being twelve-, six-, and four-membered in pyrosomalite, and seven-, six-, and five-membered in bementite. Manganese has a similar local structure in the two modulated Mn layer silicates and, therefore, manganpyrosomalite can be considered to be representative of this group of minerals.

The overlay plot of the RSFs for the scale sample and manganpyrosomalite presented in Figure 10a reveals interesting similarities in the two structures. The two structures clearly possess the same type of metal shells, with all the Mn-(Mn,Si) distances being shrunk in the unknown as indicated by the leftward shift of the magnitude and imaginary part of peaks B, C, D, and E. Peak B in the reference is broadened toward higher $R+\Delta R$ values, and this feature resulted in a wave beating at 10 \AA^{-1} in the k space (Fig. 10b). This node was correctly reproduced by assuming a first subshell of 4.2 Mn atoms at 3.27 \AA and a second of 4.8 Mn at 3.43 \AA (Fig. 10c). As expected from crystallography (Table 2), this structural model provided an approximate fit to the χ function at low k , and the addition of an Si1 shell at 3.44 \AA yielded good spectral agreement over the whole k range (Fig. 10d). The fact that the χ function of the unknown and the reference have the same wave amplitude and envelope at $k < 6 \text{ \AA}^{-1}$ suggests that they have a similar Mn-Si contribution (Fig. 10b). So far, the argument in support of the Si shell has been only moderately compelling because in layer metal silicates, the contribution of the nearest Si shell is weak and almost completely masked by the predominant metal shell contribution across octahedral edges. Strong support for the existence of Mn octahedra-Si tetrahedra corner linkages in the unknown sample comes from the analysis of peak C. In manganpyrosomalite, this peak arises from the next-nearest Si

FIGURE 9. Polyhedral representations of the manganpyrosomalite $[(\text{Mn},\text{Fe})_8\text{Si}_6\text{O}_{15}(\text{OH},\text{Cl})_{10}]$ structure showing the layer structure (upper sketch) and the planar structure (middle and lower sketch). In a same silicate sheet, SiO_4 tetrahedra (dark gray) are turned upside down, yielding a modulated structure. In the middle sketch, only SiO_4 tetrahedra pointing downward the Mn layer (light gray) are represented, whereas in the lower sketch all octahedra of the silicate sheet are drawn. After Takéuchi et al. (1969).



shell only, because the second Mn shell (peak D) is at $5.7\text{--}5.9 \text{ \AA}$. The higher O shells are weak scatterers and too disordered to contribute to peak C. In the unknown, peak C is left-shifted to slightly shorter distance. The fact that both the magnitude and the imaginary part of the Fourier transform are translated simultaneously by the same amount means that this peak also arises from Si in the unknown. Furthermore, the reduction in distance of the Si2 shell in the Mn scale sample is consistent with the observed shortening of all the Mn-Mn distances as attested by the displacement toward lower $R + \Delta R$ values of peaks B, D, and E in comparison to manganpyrosomalite.

Evidence for Mn hydrous silicate domains in the scale precipitate

IR spectroscopy shows a weak peak at $600\text{--}650 \text{ cm}^{-1}$, which was assigned to the Mn-OH vibration in layer silicate structure by comparison with the IR spectra of phyllosilicates. Thus, this peak in the IR spectrum of the scale sample indicates that Mn atoms are directly bonded to hydroxyls and have a phyllosilicate-like short-range structural order. This interpretation is consistent with chemical analysis and X-ray microfluorescence data, which showed that the Mn/Si atomic ratio of the manganoan area (1.2 ± 0.4) compares closely to those of 2:1 and 1:1 phyllosilicates. The screening by EXAFS spectroscopy of the local structure of Mn in different families of Mn silicates showed that, in the unknown sample, Mn octahedra are joined along edges and linked to SiO_4 tetrahedra by corners as in hydrous silicates. Therefore, Mn atoms are not present as individual interstitial ions in the siliceous scale matrix, but are segregated in locally ordered domains of sufficient size and abundance to be evident by X-ray diffraction. This latter technique revealed that the scale precipitate contains

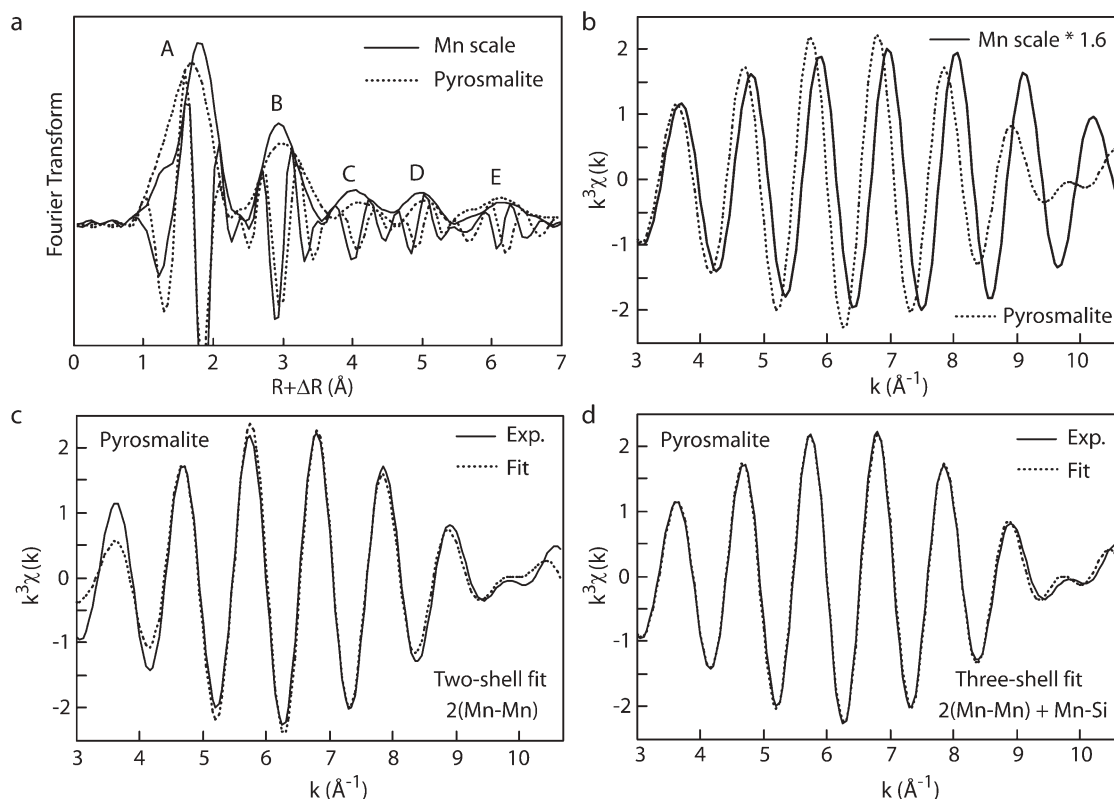


FIGURE 10. (a) Comparison of the Fourier transforms for the scale sample and manganpyrosmalite. (b) Fourier-filtered contributions to EXAFS of the nearest cationic shells for the scale sample and manganpyrosmalite. (c) Two-shell fit for manganpyrosmalite assuming $N_{\text{Mn1a}} = 4.2$, $\sigma = 0.07 \text{ \AA}$, and $R_{\text{Mn1a}} = 3.27 \text{ \AA}$, $N_{\text{Mn1b}} = 4.8$, $\sigma = 0.07 \text{ \AA}$, and $R_{\text{Mn1a}} = 3.43 \text{ \AA}$. (d) Three-shell fit for manganpyrosmalite assuming $N_{\text{Mn1a}} = 2.6$, $\sigma = 0.04 \text{ \AA}$, and $R_{\text{Mn1a}} = 3.25 \text{ \AA}$, $N_{\text{Mn1b}} = 5.6$, $\sigma = 0.04 \text{ \AA}$, $R_{\text{Mn1a}} = 3.42 \text{ \AA}$, $N_{\text{Si1}} = 4.2$, $\sigma = 0.04 \text{ \AA}$, $R_{\text{Si1}} = 3.44 \text{ \AA}$. The $R + \Delta R$ window for the inverse Fourier transform is $[2.4\text{--}3.7] \text{ \AA}$.

nanometer-sized, two-dimensional structural units, whose a and b parameters ($a = 5.44$; $b = 9.63 \text{ \AA}$ in orthogonal setting) are consistent with sheet silicates. Hazen and Wones (1972) studied the limit of strain of 2:1 trioctahedral phyllosilicates induced by the inherent differences in the lateral dimensions of the tetrahedral and octahedral sheets. For a pure Si tetrahedral sheet, they found that homogeneous sheet silicates could not be synthesized with divalent metal cations having ionic radii greater than $0.70\text{--}0.72 \text{ \AA}$. As Mn^{2+} is bigger (0.82 \AA), the lateral mismatch between the octahedral and tetrahedral sheets is alleviated in all the Mn silicate reference considered (rhodonite, pyroxmangite, and manganpyrosmalite), and also in the 1:1 Mn phyllosilicate caryopilite (Guggenheim and Eggleton 1998), by inverting certain tetrahedra and rebonding the apices in different ribbon-like and ring-like patterns. The local structure of the hydrous Mn silicate domains possibly differs from those of the crystalline references in having continuous siloxane sheets over a few tens of angstroms. This interpretation is supported by the overall similarity of the short-range ordering of Mn in the scale sample and in manganpyrosmalite, which has isolated six-membered SiO_4 rings on each side of the Mn layer. The major structural difference detected by EXAFS between these two compounds lies in the shortening of the Mn-Mn1, Mn-Mn2, Mn-Mn3, and Mn-Si2 interatomic distances in the scale sample. This reduction means that the lateral size of the Mn layer is smaller, as is

the case when an (oxyhydr)oxide layer is overlain by one or two continuous tetrahedral SiO_4 sheets like in regular 1:1 and 2:1 phyllosilicates. The strain induced by the shrinkage of the $\text{Mn}(\text{O},\text{OH})_2$ layer would be alleviated then by the small size of the hydrous Mn silicate domains. In other words, although pure large crystals of Mn phyllosilicate are unstable, nanometer-sized layers of this compound may be stabilized by reacting divalent Mn and silica at medium temperature and pressure ($152 \text{ }^\circ\text{C}$ and 690 kPa) in the laboratory and in the field during brine flashing. Also, the somewhat alkaline pH of the brine upon the scale precipitation is consistent with the formation of clay-like Mn domains as a large body of work showed that phyllosilicates readily form upon reacting aqueous metal with sodium silicate solution or silica in basic condition (Decarreau 1985; Clause et al. 1992; Badiei and Bonneviot 1998; Manceau et al. 1999; Gallup et al. 2003).

ACKNOWLEDGMENTS

The authors thank A. Decarreau and S. Guggenheim for their scientific and editorial comments.

REFERENCES CITED

- Badiei, A.R. and Bonneviot, L. (1998) Modification of mesoporous silica by direct template ion exchange using cobalt complexes. *Inorganic Chemistry*, 37, 4142–4145.
- Bailey, S.W. (1988) Hydrous phyllosilicates. 725 p. *Reviews in Mineralogy*, Mineralogical Society of America, Washington, D.C.

- Bargar, J.R., Tebo, B.M., and Villinski, J.E. (2000) In situ characterization of Mn(II) oxidation by spores of the marine *Bacillus* sp. strain SG-1. *Geochimica et Cosmochimica Acta*, 64, 2775–2778.
- Brindley, G.W. and Brown, G. (1980) Crystal structures of clay minerals and their X-ray identification. 495 p. Mineralogical Society, London.
- Clause, O., Kermarec, M., Bonneviot, L., Villain, F., and Che, M. (1992) Nickel(II) ion-support interactions as a function of preparation method of silica-supported nickel materials. *Journal of the American Chemical Society*, 114, 4709–4717.
- Decarreau, A. (1985) Partitioning of divalent transition elements between octahedral sheets of trioctahedral smectites and water. *Geochimica et Cosmochimica Acta*, 49, 1537–1544.
- Decarreau, A., Colin, F., Herbillon, A., Manceau, A., Nahon, D., Paquet, H., and Trauth-Badaud, D. (1987) Domains segregation in Ni-Fe-Mg bearing smectites. *Clays and Clay Minerals*, 35, 1–10.
- Decarreau, A., Grauby, O., and Petit, S. (1992) The actual distribution of octahedral cations in 2:1 clay minerals: results from clay synthesis. *Applied Clay Science*, 7, 147–167.
- Etchepare, J., Merian, M., and Smetankine, L. (1974) Vibrational normal modes of SiO₂. I. α and β quartz. *Journal of Chemical Physics*, 60, 1873–1876.
- Etchepare, J., Merian, M., and Kaplan, P. (1978) Vibrational normal modes of SiO₂. II. Cristobalite and tridymite. *Journal of Chemical Physics*, 68, 1531–1537.
- Fournier, R.O. (1985) The behavior of silica in hydrothermal solutions. *Reviews in Economic Geology*, 2, 45–61.
- Freed, R.L., Rouse, R.C., and Peacor, D.R. (1993) Ribbeite, a second example of edge-sharing silicate tetrahedra in the leucophoenicite group. *American Mineralogist*, 78, 190–194.
- Fujino, K., Sasaki, S., Takéuchi, Y., and Sadanaga, R. (1981) X-ray determination of electron distributions in forsterite, fayalite and tephroite. *Acta Crystallographica*, B 37, 513–518.
- Gallup, D.L. (1998) Aluminum silicate scale formation and inhibition (2); scale solubilities and laboratory and field inhibition tests. *Geothermics*, 27, 485–501.
- Gallup, D.L., Sugiaman, F., Capuno, V., and Manceau, A. (2003) Laboratory investigation of silica removal from geothermal brines to control silica scaling and produce usable silicates. *Applied Geochemistry*, 18, 1597–1612.
- Gerard, P. and Herbillon, A.J. (1983) Infrared studies of Ni-bearing clay minerals of the kerolite-pimelite series. *Clays and Clay Minerals*, 31, 143–151.
- Guggenheim, S. and Eggleton, R.A. (1987) Modulated 2:1 layer silicates: Review, systematics and predictions. *American Mineralogist*, 72, 726–740.
- — — (1988) Crystal chemistry, classification, and identification of modulated layer silicates. In G.W. Bailey, Ed., *Hydrous phyllosilicates exclusive of the micas*, 19, p. 675–725. *Reviews in Mineralogy, Mineralogical Society of America, Washington, D.C.*
- — — (1998) The crystal structures of greenalite and caryopilite: A system with long-range, in-plane structural disorder in the tetrahedral sheet. *Canadian Mineralogist*, 36, 163–179.
- Graetsch, H. (2002) Structural characteristics of opaline and microcrystalline opal materials. In P.J. Heaney, and C.T. Prewitt, Eds. *Silica. Physical behavior, geochemistry, and materials applications*, 29, p. 209–232. *Mineralogical Society of America, Washington, DC.*
- Graetsch, H., Gies, H., and Topalovic, I. (1994) NMR, XRD and IR study on microcrystalline opals. *Physics and Chemistry of Minerals*, 21, 166–175.
- Hazen, R.M. and Wones, D.R. (1972) The effect of cation substitutions on the physical properties of trioctahedral micas. *American Mineralogist*, 57, 103–109.
- Heinrich, A.R., Eggleton, R.A., and Guggenheim, S. (1994) Structure and polytypism of bementite, a modulated layer silicate. *American Mineralogist*, 79, 91–106.
- Jones, J.B. and Segnit, E.R. (1971) The nature of opal. I. Nomenclature and constituent phases. *Journal of the Geological Society of Australia*, 18, 57–68.
- Kermarec, M., Carriat, J.Y., Burattin, P., Che, M., and Decarreau, A. (1994) FTIR identification of the supported phases produced in the preparation of silica-supported nickel catalysts. *Journal of Physical Chemistry*, 98, 12007–12017.
- Manceau, A. and Calas, G. (1986) Ni-bearing clay minerals. 2. X-ray absorption study of Ni-Mg distribution. *Clay Minerals*, 21, 341–360.
- Manceau, A., Gallup, D., Ildefonso, P., Hazemann, J.L., and Flank, A.M. (1995) Crystal chemistry of hydrous iron silicate scales deposits at the Salton Sea Geothermal field. *Clays and Clay Minerals*, 43, 304–317.
- Manceau, A., Chateigner, D., and Gates, W.P. (1998) Polarized EXAFS, distance-valence least-squares modeling (DVLS) and quantitative texture analysis approaches to the structural refinement of Garfield nontronite. *Physics and Chemistry of Minerals*, 25, 347–365.
- Manceau, A., Schlegel, M., Nagy, K.L., and Charlet, L. (1999) Evidence for the formation of trioctahedral clay upon sorption of Co²⁺ on quartz. *Journal of Colloid and Interface Science*, 220, 181–197.
- Manceau, A., Schlegel, M.L., Musso, M., Sole, V.A., Gauthier, C., Petit, P.E., and Trolard, F. (2000) Crystal chemistry of trace elements in natural and synthetic goethite. *Geochimica et Cosmochimica Acta*, 64, 3643–3661.
- Moenke, H.H.W. (1974) Silica, the three dimensional silicates, borosilicates and beryllium silicates. In V.C. Farmer, Ed. *The infrared spectra of minerals*, 4, p. 365–382. *Mineralogical Society Monograph*, London.
- Moore, P.B. (1970) Edge-sharing silicate tetrahedra in the crystal structure of leucophoenicite. *American Mineralogist*, 55, 1146–1165.
- Nagata, H., Shimoda, S., and Sudo, T. (1974) On dehydration of bound water of sepiolite. *Clays and Clay Minerals*, 22, 285–293.
- Narita, H., Koto, K., and Morimoto, N. (1977) The crystal structures of MnSiO₃ polymorphs (rhodonite- and pyroxmangite-type). *Mineralogical Journal*, 8, 329–342.
- Norlund, C.A. (1965) A single crystal x-ray diffraction study of Mn(OH)₂. *Acta Chemica Scandinavica*, 1765–1788.
- O'Day, P.A., Rehr, J.J., Zabinsky, S.I., and Brown, G.E., Jr. (1994) Extended x-ray absorption fine structure (EXAFS) analysis of disorder and multiple-scattering in complex crystalline solids. *Journal of the American Chemical Society*, 116, 2938–2949.
- Pinkney, L.R. and Burnham, C.W. (1988) Effects of compositional variation on the crystal structures of pyroxmangite and rhodonite. *American Mineralogist*, 73, 798–808.
- Rehr, J.J., Mustre de Leon, J., Zabinsky, S.I., and Albers, R.C. (1991) Theoretical X-ray Absorption Fine Structure Standards. *Journal of the American Chemical Society*, 113, 5135–5145.
- Ressler, T. (1998) WinXAS: a Program for X-ray Absorption Spectroscopy Data Analysis under MS-Windows. *Journal of Synchrotron Radiation*, 5, 118–122.
- Rossman, G.R. (1988) Optical spectroscopy. In F.C. Hawthorne, Ed., *Spectroscopic methods in mineralogy and geology*, 18, p. 207–254. *Reviews in Mineralogy, Mineralogical Society of America, Washington D.C.*
- Russell, J.D., Farmer, V.C., and Velde, B. (1970) Replacement of OH by OD in layer silicates and identification of the vibrations of these groups in infrared spectra. *Mineralogical Magazine*, 37, 869–979.
- Spycher, N.F. and Reed, M.H. (1989) Evolution of a Broadlands-type epithermal ore fluid along alternative P-T paths: implications for the transport and deposition of base, precious and volatile metals. *Economic Geology*, 84, 328–359.
- Takéuchi, Y., Kawada, I., Irizimiri, S., and Sadanaga, R. (1969) The crystal structure and polytypism of manganpyrosmalite. *Mineralogical Journal*, 5, 450–467.
- Teo, B.K. (1986) EXAFS: basic principles and data analysis. 349 p. Springer-Verlag, Berlin.
- Webb, J.A. and Finlayson, B.L. (1987) Incorporation of Al, Mg, and water in opal-A: Evidence from speleotherms. *American Mineralogist*, 72, 1204–1210.
- Wilkins, R.W.T. and Ito, J. (1967) Infrared spectra of some synthetic talcs. *American Mineralogist*, 52, 1649–1661.
- Wollast, R., Mackenzie, F.T., and Bricker, O.P. (1968) Experimental precipitation and genesis of sepiolite at earth-surface conditions. *American Mineralogist*, 53, 1645–1662.
- Yeniyoğlu, M. (1986) Vein-like sepiolite occurrence as a replacement of magnesite in Konya, Turkey. *Clays and Clay Minerals*, 34, 353–356.

MANUSCRIPT RECEIVED JANUARY 9, 2004

MANUSCRIPT ACCEPTED SEPTEMBER 10, 2004

MANUSCRIPT HANDLED BY BERTRAND DEVOUARD